Hollow spheres of nanocarbon and their manganese dioxide hybrids derived from soft template for supercapacitor application

Zheng-Chun Yang [a], Chun-Hua Tang [a], Hao Gong [a], Xu Li [b,**], John Wang [a,*]

[a] Department of Materials Science and Engineering, National University of Singapore, Singapore 117574, Singapore
[b] Institute of Materials Research and Engineering (IMRE), Singapore 117602, Singapore

HIGHLIGHTS

- Hollow spheres of nanocarbon have been successfully synthesized.
- Hollow spheres of nanocarbon exhibit both micro- and meso-pores in the carbon wall.
- Hollow spheres of carbon–MnO$_2$ hybrid are formed by the redox reaction.
- Double MnO$_2$ layers are grown on the external and internal surfaces of hollow carbon.
- Hollow spheres of carbon–MnO$_2$ hybrids are promising for supercapacitor applications.

ARTICLE INFO

ABSTRACT

A facile soft templating strategy has been developed for synthesizing hollow spheres of nanocarbon by hydrothermal process. In this soft templating strategy, poly (ethylene oxide)–poly (propylene oxide)–poly (ethylene oxide) block co-polymers are used as the template while α-cyclodextrin are employed as the carbon precursor. After hydrothermal treatment, the soft templates can be easily removed by pyrolysis of the as-prepared hollow spheres in argon. The resultant hollow spheres of nanocarbon exhibit both micro- and meso-pores in carbon wall with a specific surface area of ∼380 m^2 g^{-1}. Upon incorporation of permanganate (MnO$_4^-$) into the hollow carbon spheres, nanocrystalline manganese dioxide (MnO$_2$) is grown on the carbon surface, where the redox reaction between carbon and MnO$_4^-$ takes place, giving rise to the formation of hollow carbon–MnO$_2$ hybrid particles. An appropriate control in the diffusion of MnO$_4^-$ into the core of hollow carbon spheres, nanocrystalline MnO$_2$ can be successfully grown on both the external and internal surfaces of the hollow carbon structure. The carbon–MnO$_2$ hybrid spheres are demonstrated as a promising candidate material for supercapacitor application.

© 2013 Elsevier B.V. All rights reserved.

1. Introduction

For the past two decades, supercapacitors have received considerable attention, owing to their high power density, extremely long cycle life and fast charging–discharging rates, which are required by a wide spectrum of applications in load-leveling power sources, premium power systems, fast switches, consumer electronics, battery-power operations and military devices [1–3]. Supercapacitors are broadly grouped into two types, depending on the charge storage mechanisms, i.e., charge storage by electrical double layers and pseudocapacitance making use of the surface redox reaction of certain transitional metal oxides such as manganese dioxide (MnO$_2$) [4–6]. For both types of supercapacitors, various carbon-based materials have been used as electrodes, including for example active carbons, carbon aerogels, nanofoams, carbon nanotubes and more recently graphene [3,7–13]. Porous carbon-based materials are particularly interesting due to their relatively stable pore structure, high specific surface area, controllable pore size distribution, chemical stability and high electrical conductivity [14].

Among the porous carbon-based materials, carbon aerogels and nanofoams have been prepared by sol–gel process [7–10,15–22]. In these template-free processes, organic precursors, such as resorcinol, formaldehyde and styrene, are employed as the carbon source. The designed porous architecture is controlled by sol–gel chemistry and subsequent pyrolysis at high temperature [15–22].

To better control the porous architecture of carbon-based materials, both hard template and soft template strategies have been developed [23]. In the hard template strategy, solid inorganic materials of controlled size and morphology, such as zinc oxide, aluminosilicate and mesoporous silica are employed as the hard templates [24–28], whereby the resultant morphologies and pore size distributions can be tuned. An appropriate carbon precursor, such as phenol formaldehyde resin, carbohydrates, dopamine and furfuryl alcohol is introduced on the hard template surface by adsorption or impregnation [29–32]. The carbon precursor/hard template hybrids are then subjected to pyrolysis treatment at high temperature under a controlled atmosphere to convert the precursor into wanted carbon [33]. The hard templates are subsequently etched off using sodium hydroxide or hydrogen fluoride to obtain the designed porous carbon structure [23,28,34]. Undoubtedly the hard template strategy is an effective approach for synthesis of porous carbons with controllable pore sizes and morphologies [26,35]. It however requires the pre-fabrication of hard templates and their subsequent removal, making a typical multiple-step process. In contrast, in the soft template strategy, surfactants and block co-polymers are employed as the soft templates, which can generate various nano- and meso-structures by the hydrophobic/hydrophilic interactions and hydrogen bonding in aqueous solution, including micelles, cylindrical, lamellar and vesicle structures [23,36]. Organic precursors, such as polystyrene, resorcinol formaldehyde and carbohydrates are incorporated into the soft template. Both the precursor and soft templates can be converted into porous carbon structures by carbonization at high temperature [37–39].

To improve the overall performance of supercapacitors, considerable efforts have been made with the development of carbon-transitional metal oxide nanocomposites, where the storage by electrical double layers is combined with the pseudocapacitance. For this purpose, several transitional metal oxides that can undergo surface redox reactions, such as ruthenium oxide [40] and MnO_2 [41], have been studied. Although the combination of non-Faradaic and Faradaic charge storages can in principle lead to much improved performance, the capacitance values reported so far for the carbon-transitional metal oxide nanocomposites is well below the theoretical prediction. It would therefore be of considerable interest to further investigate the hybrid structure consisting of porous carbon and transitional metal oxide spheres, by devising new synthesis process for them and understand their performance in supercapacitors.

In this paper, a facile synthesis route based on the soft template approach for forming hollow spheres of nanocarbon with the desired porous structure and their nanohybrid with MnO_2 nanoparticles is described. Poly (ethylene oxide)–poly (propylene oxide)–poly (ethylene oxide) (PEO–PPO–PEO) co-polymers have been studied as soft templates for several types of mesoporous materials [23]. Block co-polymer F127, which is PEO_{106}–PPO_{70}–PEO_{106}, is chosen as the soft template by considering its environment friendliness and commercial availability. The α-cyclodextrin (α-CD) is used as the carbon precursor for synthesis of the hollow nanocarbon spheres by hydrothermal reaction and subsequent pyrolysis treatment. In the process, both the carbon precursor and F127 are converted into nanocarbon in the hollow spheres, generating the desired micro- and meso-porosities [42]. The MnO_2 is chosen for development of the wanted pseudocapacitance, by considering its high theoretical specific capacitance (1370 F g^{-1}) and environmental friendliness [1]. The MnO_2 nanocrystals are incorporated into the micro- and meso-carbon structures, by successfully growing them on the porous carbon surface through the redox reaction between potassium permanganate ($KMnO_4$) and carbon in aqueous solution. By carefully controlling the processing parameters involved, the MnO_2 nanocrystals can be grown on both

the external and internal surfaces of hollow nanocarbon spheres, leading to a more electrochemically active electrode surface.

2. Experimental

2.1. Materials

The F127 used in this project is purchased from Sigma–Aldrich Company, and α-CD from Tokyo Chemical Industry Company. The $KMnO_4$ for this project is purchased from Alfa Aesar Company.

2.2. Synthesis of hollow spheres of nanocarbon

To synthesize the hollow carbon spheres, 30 mg F127 was firstly dissolved in 20 mL deionized (DI) water. 60 mg of α-CD was then dissolved in 20 mL DI water. Upon complete dissolution of F127 and α-CD forming respective clear solutions, the α-CD solution was injected into the solution of F127 under stirring at 700 rpm. The mixed solution was stirred overnight and then transferred into a Teflon sealed autoclave tube. Upon the completion of hydrothermal treatment at 200 °C for 6 h, the clear solution turned into black in appearance. The black solution was then washed by DI water three times by centrifugation at 9000 rpm for 30 min. After washing, the black precipitates were re-dispersed in DI water and freeze dried for two days to obtain the carbon powder for further study, which was denoted as HCS. Finally, the dry powder of the as-prepared sample was further pyrolyzed in a tube furnace at 500 °C for 30 min under argon (Ar) gas protection, which was denoted as HCSA.

2.3. Synthesis of hollow carbon–MnO_2 hybrids

For incorporation of nanocrystalline MnO_2 into the hollow spheres of porous carbon, i.e., on the surface of HCSA, the direct redox reaction of $KMnO_4$ on carbon surface was employed. Typically, 30 mg of HCSA was ultrasonically dispersed in 50 mL DI water. 90 mg $KMnO_4$ was then added into the HCSA dispersion. After stirring for an appropriate period of time, e.g., 5 min and 16 h, the mixed solution was heated to 70 °C. After refluxing at 70 °C for 180 min, the black precipitates were washed three times by centrifugation at 9000 rpm for 10 min. Finally, the product was collected after drying in vacuum oven at 60 °C for 2 days. The hybrid materials thus obtained were denoted as HCSA/MnO_2-5 min and HCSA/MnO_2-16 h to differentiate the difference in stirring time, i.e., 5 min and 16 h, respectively.

2.4. Characterization

The morphology and structure of the hollow nanocarbon spheres and their hybrids were studied by using scanning electron microscopy (SEM; XL 30 FEG-SEM Philips) and transmission electron microscopy (TEM; CM 300 FEG-Philips). Fourier transform infrared (FTIR) spectra were acquired by using Perkin Elmer FT-IR 2000 spectrometer, where the sample was prepared by pressing the mixture of the sample powder and potassium bromide into a thin disk. Nitrogen (N_2) adsorption and desorption isotherms were measured at −196 °C by using a Micromeritics ASAP 2020 system. In addition, the specific surface area was determined by Brunauer–Emmett–Teller (BET) method and the pore size distribution was calculated using the nonlocal density functional theory (NLDFT) method. Raman spectra were acquired by using RENISHAW Raman Microscope with 514 nm laser radiation source. X-ray diffraction (XRD) phase analysis was conducted by using Bruker D8 XRD, which was equipped with Cu Kα radiation ($\lambda = 0.15418$ nm). X-ray photoelectron spectroscopy (XPS) studies were conducted using an

AXIS Ultra spectrometer (Kratos Analytical), which was equipped a monochromatized Al Kα X-ray source. The elemental distribution in the sample was studied using a scanning TEM-energy dispersive X-ray spectroscopy (STEM-EDX; JEOL 2100). The loading of MnO_2 in hollow carbon spheres was determined by Inductively Coupled Plasma (ICP) Analysis using Perkin Elmer Dual-view Optima 5300 DV ICP-OES system.

2.5. Electrochemical measurement

Electrochemical performance of the $HCSA/MnO_2$-5 min and $HCSA/MnO_2$-16 h as electrodes in supercapacitor were investigated. The working electrode was fabricated by coating the viscous slurry of active materials (80 wt. %), carbon black (10 wt. %), and poly-tetrafluoroethylene (10 wt. %) in ethanol onto a Ni foam of 4 cm^2 in area and 1 mm in thickness. After drying in a vacuum oven at 120 °C for 12 h, the coated Ni foam was uniaxially pressed under a pressure of 49 MPa to enhance the adhesion between the active materials and the Ni foam. The loading of active material on the Ni foam was determined to be 8.9 mg and 8.0 mg for $HCSA/MnO_2$-5 min and $HCSA/MnO_2$-16 h, respectively. A series of electrochemical parameters of the as-fabricated working electrode were tested, including the cyclic voltammetry (CV) and galvanostatic charge–discharge, using a three-electrode compartment on a Solartron Electrochemical System SI 1287. In the three-electrode system, aqueous sodium sulfate (Na_2SO_4) solution of 1.0 M in concentration, Pt foil and Ag/AgCl electrode were used as the electrolyte, counter electrode and reference electrode, respectively. The electrolyte was purged with N_2 to remove oxygen.

3. Results and discussions

3.1. Characterizations of HCS and HCSA

From the SEM image shown in Fig. 1(a), the as-prepared particles appear to exhibit a largely spherical morphology with an average diameter of ∼400 nm. In addition, as shown in Fig. 1(b), which is a TEM image, the as-prepared HCS exhibit a well established hollow structure. Moreover, according to the SEM and TEM images (Fig. 1(c) and (d)) for the pyrolyzed sample (HCSA), there is little change in the morphology when compared to the sample before pyrolysis. Indeed, as shown Fig. 1(d), the hollow spherical structure is well preserved during the pyrolysis treatment. The particle surface of HCSA however appears coarse, as compared to that of HCS. As discussed later, the change in surface roughness is due to the decomposition of F127 at the pyrolysis temperature.

The surface characteristics of HCS and decomposition of F127 at the pyrolysis temperature are further confirmed by the FTIR results, as shown in Fig. 2. Comparing the FTIR spectra between the as-prepared HCS and α-CD, the carbonization of α-CD during the hydrothermal process is verified, as shown by the appearance of C=C vibration bands at 1635 cm^{-1} [43]. In addition, after hydrothermal treatment, there are hydroxyl and carboxyl functional groups observed on the hollow particle surface, as demonstrated by the
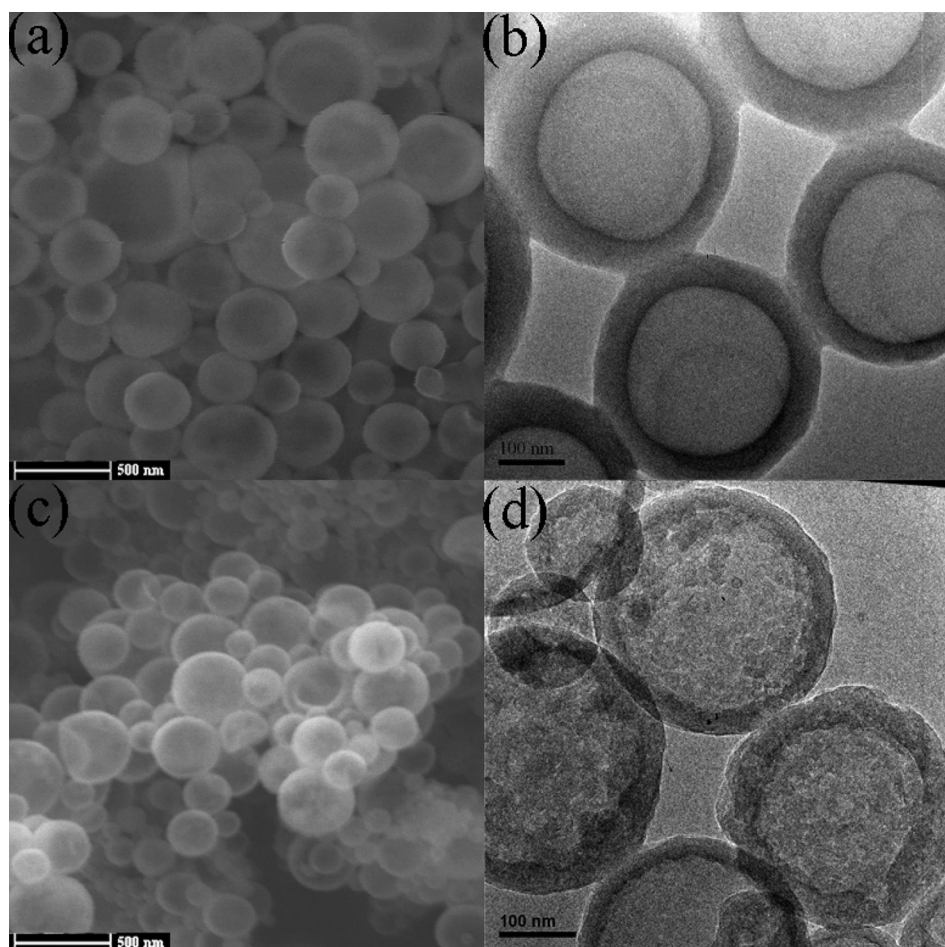

Fig. 1. SEM and TEM images of HCS (a and b), and HCSA (c and d), derived from hydrothermal treatment of α-CD in the presence of 30 mg F127, before and after the pyrolysis.
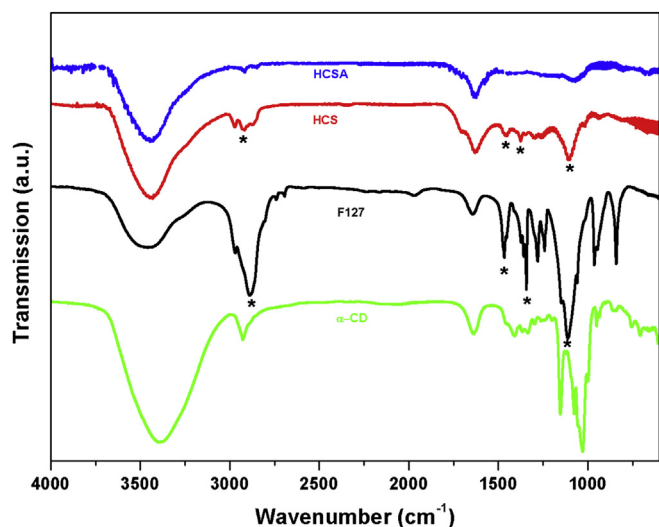
Fig. 2. FTIR spectra of α-CD, F127, HCS and HCSA.

vibration bands at 3440 and 1704 cm^{-1}, respectively [43]. Interestingly, the FTIR spectra in Fig. 2 show that F127 is well preserved under the hydrothermal condition. The presence of hydrophilic PEO blocks on the surface of the as-prepared HCS is demonstrated by the characteristic bands of 2890, 1465, 1343 and 1109 cm^{-1}, which are seen in the FTIR spectra of both F127 and HCS (labeled * in Fig. 2) [44]. Moreover, a detailed comparison of FTIR spectra among HCSA, HCS and F127 confirms that F127 is largely decomposed by the pyrolysis treatment, as the characteristic bands of F127 block copolymer have disappeared from the FTIR spectra of HCSA.

The N$_2$ adsorption/desorption isotherms and the NLDFT pore size distribution calculated for HCS and HCSA are shown in Fig. 3. Only negligible N$_2$ adsorption occurred in the relative pressure (P/P_0) range of 0–0.9, confirming the largely nonporous nature of the particle wall before pyrolysis. As discussed above, the molecular structure of F127 is largely preserved under the hydrothermal condition, and is present in HCS, as demonstrated by the FTIR analysis. As a result, the specific BET surface area (12.9 m^2 g^{-1}) measured for HCS is rather low, due to the presence of PEO chains on the particle surface, which block off the porosity in the wall
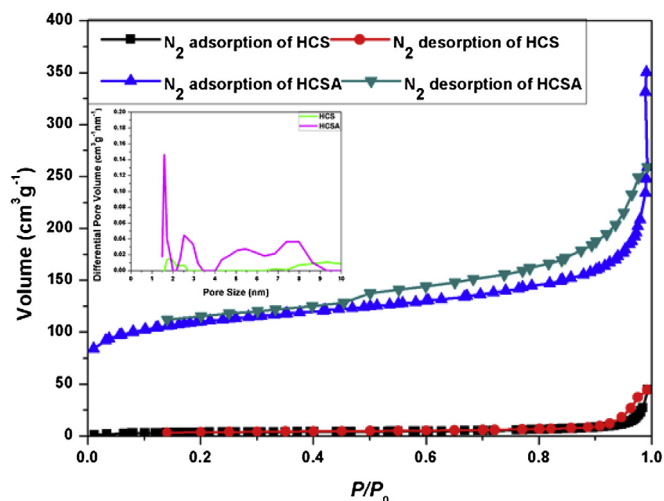
thickness if any [42]. Upon pyrolysis at high temperature in Ar, the molecular structure of F127 previously retained in HCS is decomposed, generating pores on the surface and across the carbon wall thickness. Indeed, it is confirmed by the BET surface analysis, which is shown in Fig. 3. HCSA exhibits a much higher specific surface area of 379 m^2 g^{-1} than that of HCS. In the isotherm curves of HCSA, a linear increase in N$_2$ adsorption occurs in the lower pressure range of ($P/P_0 = 0.05$–0.25) due to the monolayer adsorption of N$_2$ molecules in the micro- and meso-pores, which give rise to the high BET surface area measured. A long plateau is then observed at high pressure of ($P/P_0 = 0.25$–0.9), due to the taking up of micro- and meso-pores. The NLDFT pore size distribution peaks at 1.5 nm, as shown by the inset in Fig. 3. Finally, a sharp increase in N$_2$ uptake at $P/P_0 = 0.9$–1.0 is observed, which corresponds to both the interparticle voids and hollow cavity in the particle center. There is a hysteresis loop appearing in the desorption branch over the pressure range of $P/P_0 = 0.4$–1.0 with two-step inflections, corresponding to N$_2$ evaporation from the inter-particle voids ($P/P_0 = 0.9$–1.0) and hollow cavity ($P/P_0 = 0.4$–0.9), respectively. The sudden closure of the hysteresis loop at $P/P_0 = 0.4$ is due to the inkbottle type of pores, which is quite typical for hollow spheres due to the delay in N$_2$ evaporation from the hollow voids blocked by the surrounding micro- and meso-pores in the carbon wall during the N$_2$ desorption process [42].

From the experimental results discussed above, it can be concluded that the hydrothermal treatment of α-CD in the presence of F127 gives rise to the formation of hollow spheres of nanocarbon. As illustrated in Fig. 4, F127 plays as an important function as the soft template for the formation of hollow structure, while α-CD undergoes carbonization to form the carbon wall. According to the surfactant phase diagram of F127, when dissolved in DI water with the designed mass concentration, which is 0.075% in the present work, it exhibits a macromolecular morphology [45]. Upon the injection of α-CD solution, the PEO chains in F127 can penetrate into the inner cavity of α-CD molecule to form an inclusion type of supermolecular complexes [46]. To demonstrate the supermolecular complexes, XRD study is conducted on the mixture of 30 mg F127 and 60 mg α-CD, prior to the hydrothermal treatment. As shown in Fig. S1, the inclusion type of supermolecular complexes formed between PEO blocks of F127 and α-CD is confirmed by the appearance of a characteristic XRD peak of the channel type crystal structure of the inclusion complex [47], detected at 19.4°, which is labeled * in Fig. S1. Moreover, as shown in Fig. S1, there is no such peak detected in the XRD trace of either F127 or α-CD. Under the hydrothermal condition of high temperature and pressure, the F127/α-CD supermolecular complexes are self-assembled due to the decrease in critical micelle concentration [48]. As the PEO chain of F127 penetrates into the inner cavity of α-CD, the hydrophobic-hydrophilic balance between the PPO block in F127 and PEO/α-CD segment enables the F127/α-CD supermolecular complexes to develop a vesicle type structure [49]. The progress of hydrothermal treatment then leads α-CD to undergo carbonization at the hydrothermal temperature and pressure [42]. Since F127 is largely retained under the hydrothermal condition due to its relatively high thermal stability, as confirmed by the FTIR analysis, it is at the pyrolysis temperature of 500 °C that F127 is decomposed generating the observed micro- and meso-pores in the carbon wall, which is shown in Fig. 4.

3.2. Characterizations of HCSA/MnO$_2$-5 min and HCSA/MnO$_2$-16 h

By the direct redox reaction, nanocrystalline MnO$_2$ is grown on the surface of HCSA. In the reaction of $4MnO_4^- + 3C + H_2O \rightarrow 4MnO_2 + CO_3^{2-} + 2HCO^{3-}$, HCSA acts as both a reduction agent and substrate to support MnO$_2$ nanocrystallites [50]. As

Fig. 3. N$_2$ adsorption/desorption isotherms of HCS and HCSA. Inset: NLDFT pore size distribution calculated for HCS and HCSA.
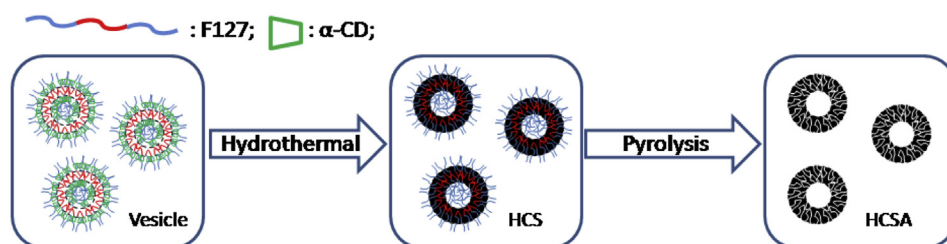
Fig. 4. A schematic illustration for the formation of hollow spheres of nanocarbon, when α-CD + F127 mixture is hydrothermally treated, followed by pyrolysis at high temperature.

shown by the SEM and TEM images (Fig. 5) for HCSA/MnO$_2$ nano-hybrids, nanocrystalline MnO$_2$ is formed and is distributed rather uniformly on the surface of the hollow carbon structure. The hollow carbon morphology is well retained, which indicates that the formation and growth of MnO$_2$ nanocrystallites have not destroyed the hollow carbon structure. The hollow sphere structure of nanocarbon is further confirmed by the results of STEM-EDX element mapping, which are shown in Fig. S2 and S3 in the supporting information. It is clearly shown by the comparison between the bright field images, Fig. S2 (a) and Fig. S3 (a), and the carbon element mapping images, Fig. S2 (b) and Fig. S3 (b). Furthermore, there is also a visible difference between the two HCSA/MnO$_2$ samples derived from different treatment durations, denoted as HCSA/MnO$_2$-5 min and HCSA/MnO$_2$-16 h respectively. According to the TEM image of HCSA/MnO$_2$-5 min shown in Fig. 5(b),

nanocrystalline MnO$_2$ largely occurs on the external surface of HCSA, which is further indicated by the STEM-EDX element mapping of manganese (Mn; Fig. S2 (d)). In contrast, for HCSA/MnO$_2$-16 h shown in Fig. 5(d), nanocrystallites of MnO$_2$ appear to occur on both the external and internal surfaces of HCSA, where there is a double layer structure for MnO$_2$. As further shown in Fig. S3 (d), Mn appears on both the external and internal carbon shell surfaces of HCSA/MnO$_2$-16 h. As discussed above, HCSA exhibits micro- and meso-pores across the carbon wall, which has been demonstrated by BET analysis results. As a result, upon the dispersion of HCSA into aqueous solution of KMnO$_4$, permanganate (MnO$_4^-$) can slowly diffuse into the interior of HCSA through the pores in the carbon wall of the hollow structure. As shown in Fig. 6, when the mixed solution is stirred for 5 min, a rather limited amount of MnO$_4^-$ is diffused into the inside of the hollow structure. Subsequent
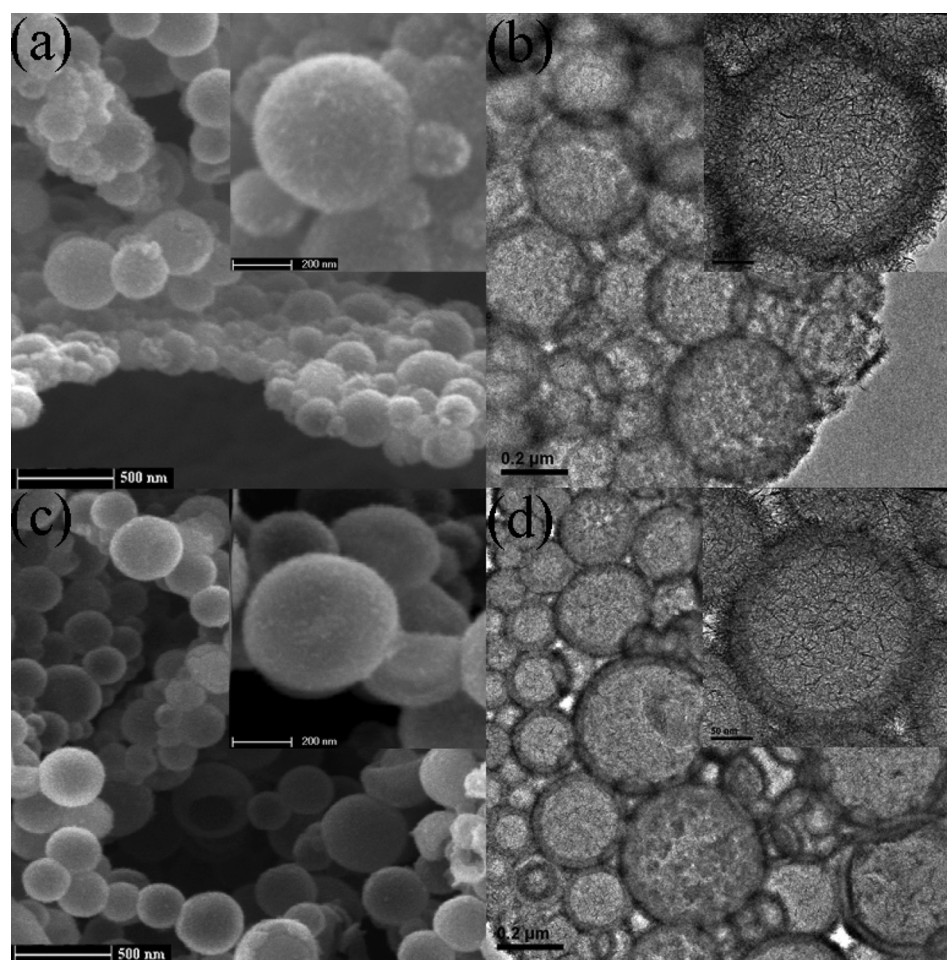

Fig. 5. SEM and TEM images of HCSA/MnO$_2$-5 min (a and b), and HCSA/MnO$_2$-16 h (c and d), showing the carbon-MnO$_2$ hybrid structure.
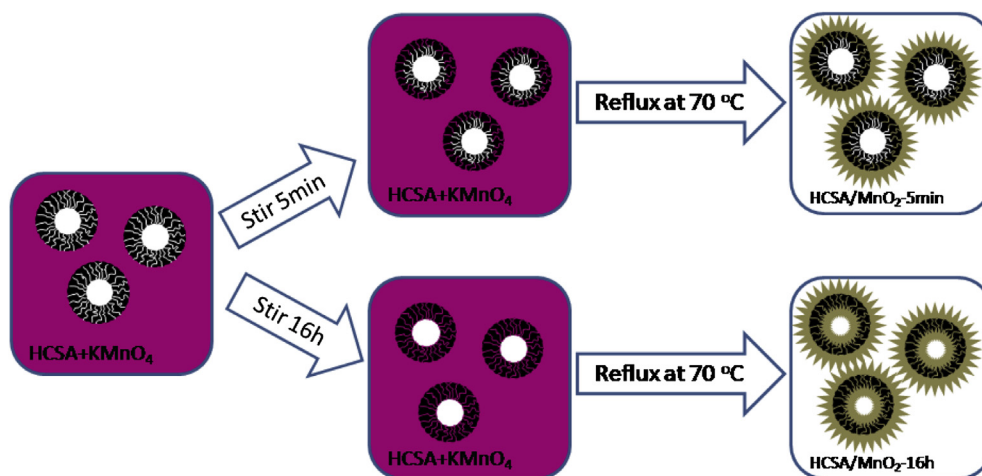
Fig. 6. A schematic illustration for the formation of HCSA/MnO$_2$-5 min and HCSA/MnO$_2$-16 h.

refluxing process leads to the formation MnO$_2$ on the external surface of hollow carbon spheres from MnO$_4^-$ by the redox reaction. In contrast, when the mixed solution is stirred for an extended duration of 16 h, considerable amount of MnO$_4^-$ is able to diffuse into the inside of the hollow structure. The subsequent conversion of MnO$_4^-$ to MnO$_2$ by redox reaction on the internal surface of carbon wall under the refluxing process generated the double layer structure, where there are nanocrystalline MnO$_2$ distributed on both the external and internal surfaces of HCSA.

ICP analysis shows that the loading of MnO$_2$ in HCSA is 25.50 wt. % and 27.42 wt. % for HCSA/MnO$_2$-5 min and HCSA/MnO$_2$-16 h, respectively. The presence of nanocrystalline MnO$_2$ on the surface of HCSA is also confirmed by XPS survey spectrum, which is shown in Fig. S4. As shown in Fig. 7 for Mn 2p spectra, the spin-orbit peaks of MnO$_2$ correspond to Mn 2p$_{2/3}$ and Mn 2p$_{1/2}$, which occur at 653.9 and 642.2 eV, respectively [51]. To further confirm the nanocrystalline structure of MnO$_2$, XRD and Raman spectra are acquired. From the XRD spectra of HCSA/MnO$_2$-5 min and HCSA/MnO$_2$-16 h, which are shown in Fig. 8, the crystalline phase of MnO$_2$ is identified to be α crystallographic form, as confirmed by the peaks at 2θ = 37° and 66°, corresponding to the (211) and (002) reflections, respectively [52]. Moreover, the Raman spectra of HCSA/MnO$_2$-

5 min, HCSA/MnO$_2$-16 h and HCSA in Fig. 9, all show the typical spectra for carbon, exemplified by the peaks at 1346 cm^{-1} (D) and 1556 cm^{-1} (G) [43]. As shown in Fig. 9, the broad peak at 1346 cm^{-1}, is assigned to D band, which corresponds to the amorphous carbon structure in the carbon particles and is associated with the benzene ring-breathing vibrations [43]. The peak at 1556 cm^{-1} appears to match well with the G band, which is a band related to the disordered graphite structure, suggesting that the occurrence of the in-plane bond-stretching motion of the C sp^2 atoms pairs [43]. Furthermore, the α phase of MnO$_2$ is confirmed by the characteristic bands in the low Raman shift region, which peak at 573 (M1) and 640 (M2) cm^{-1}, respectively [53,54]. In the MnO$_6$ groups, the Mn–O stretching vibration band within the basal plane is represented by M1, while the symmetric Mn–O stretching vibration band is related to M2 [55]. Therefore both XRD and Raman spectra confirm that the nanocrystalline MnO$_2$ phase formed on the surface of HCSA is of α phase.

3.3. Electrochemical behavior

Based on the above hollow spherical structure discussed for HCSA/MnO$_2$ hybrids, it would be of interest to study their
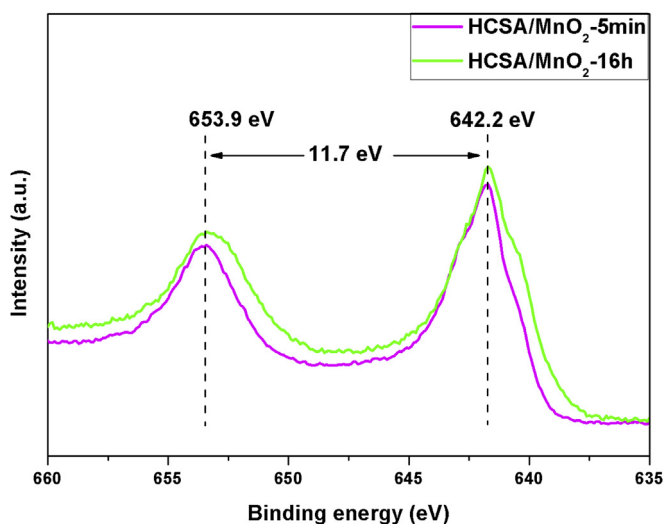

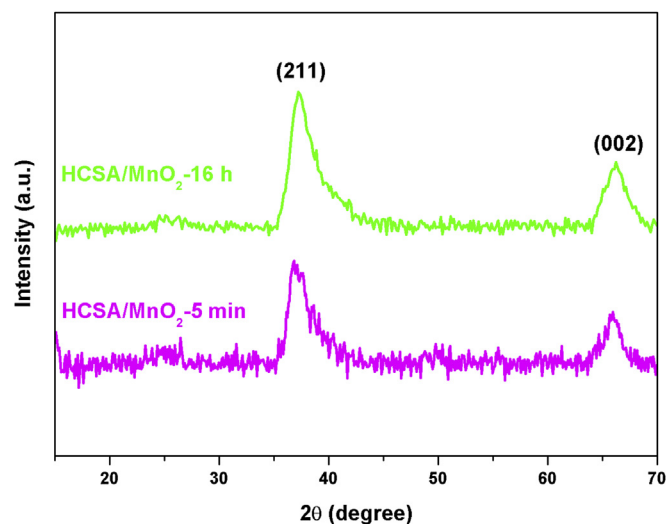Fig. 7. XPS spectra of Mn 2p for HCSA/MnO$_2$-5 min and HCSA/MnO$_2$-16 h.

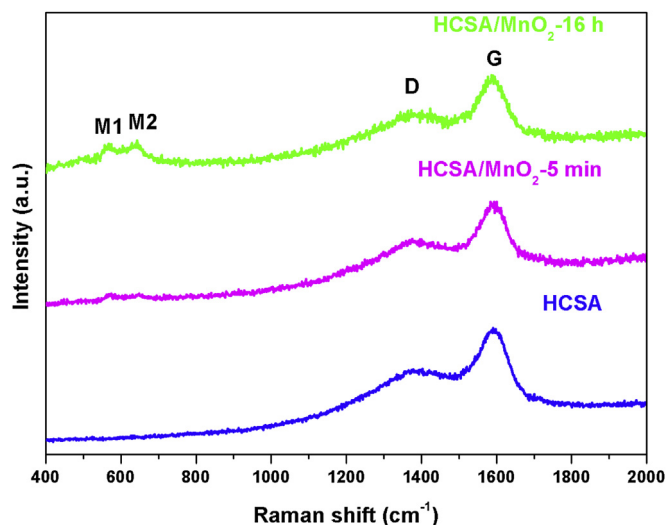Fig. 8. XRD traces of HCSA/MnO$_2$-5 min and HCSA/MnO$_2$-16 h.

Fig. 9. Raman spectra of HCSA/MnO$_2$-5 min, HCSA/MnO$_2$-16 h and HCSA.

performance as an electrode in supercapacitor, where the pseudocapacitive MnO$_2$ is combined into mesoporous carbon substrate [53]. Their electrochemical performances as electrodes in supercapacitor are studied by using a three-electrode configuration. As shown in Fig. 10(a) and (b), the CV curves of both supercapacitor working electrodes, made of HCSA/MnO$_2$-5 min and HCSA/MnO$_2$-16 h respectively, exhibit quasi-rectangular shapes in the potential window of 0–1.0 V at a variation of scan rates from 1 to 100 mV s^{-1}, which demonstrate the excellent reversibility of the supercapacitor working electrodes [56]. The MnO$_2$ nanocrystallites assembled on the surface of HCSA are expected to give rise to pseudocapacitive behavior. A careful comparison between Fig. 10(a) and (b) shows that the supercapacitor working electrode made of HCSA/MnO$_2$-16 h exhibits a higher current density than that of HCSA/MnO$_2$-5 min, suggesting that the former exhibits a higher specific capacitance. At a current density of 0.1 A g^{-1}, rather linear shape and symmetric behavior are observed in the galvanostatic charge–discharge profiles, as shown in Fig. 10(c), further demonstrating that the HCSA/MnO$_2$ hybrids exhibit a desired capacitive behavior and excellent electrochemical reversibility of Faradic reaction between sodium ion (Na$^+$) in the electrolyte and nanocrystalline MnO$_2$ on the carbon surface [53]. As shown in Fig. 5, there are MnO$_2$ nanocrystallites assembled on both the external and internal surfaces of carbon wall in HCSA/MnO$_2$-16 h, while there is MnO$_2$ only on the external surface for HCSA/MnO$_2$-5 min. Such difference in structure leads to the apparent change in supercapacitor performance. Their behavior in charge storage is further confirmed by the specific capacitance value calculated for various scan rates. As shown in Fig. 10(d), the specific capacitance of HCSA/MnO$_2$-16 h is higher than HCSA/MnO$_2$-5 min at each scan rate, which is apparently due to the more electrochemically active surface provided by the double MnO$_2$ layers on the carbon shell. At low scan rates, e.g.
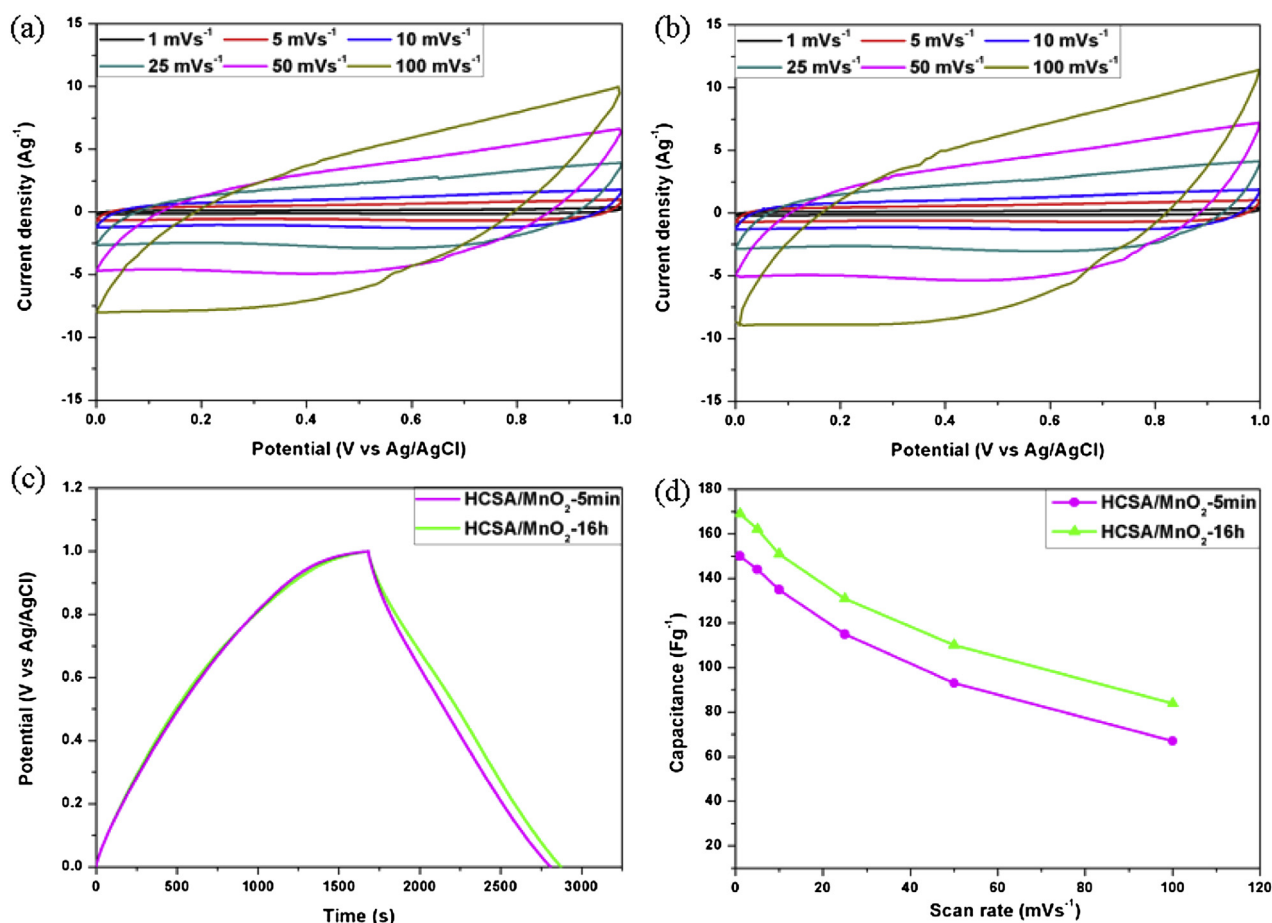

Fig. 10. Electrochemical behavior of the supercapacitor working electrode made of HCSA/MnO$_2$ hybrid. (a) CV curves of the supercapacitor working electrode made of HCSA/MnO$_2$-5 min; (b) CV curves of the supercapacitor working electrode made of HCSA/MnO$_2$-16 h; (c) galvanostatic charge-discharge of the supercapacitor working electrodes at a current density of 0.1 A g^{-1}; (d) variation in specific capacitance for the supercapacitor working electrodes against different scan rates.

1 mV s^{-1}, the specific capacitances are ∼150 and ∼170 F g^{-1} for HCSA/MnO$_2$-5 min and HCSA/MnO$_2$-16 h, respectively, which are comparable to those previously reported for MnO$_2$ based super-capacitor electrodes [57]. The lower than expected specific capacitance may well be due to the overall low electrical conductivity. The hollow carbon spheres consist of largely amorphous carbon. The MnO$_2$ is known to exhibit rather low electrical conductivity, which cover the carbon surface, and therefore the overall conductivity will be low for the carbon−MnO$_2$ nanohybrid. Another consideration is the relatively poor stability of MnO$_2$, which can undergo dissolution in the electrolyte. Due to the shortening in Na$^+$ diffusion distance into MnO$_2$ at high scan rates, the specific capacitance decreases with the scan rate [58,59]. The capacitance loss is 50.3% for the electrode made of HCSA/MnO$_2$-16 h, while it is 55.3% for the electrode made of HCSA/MnO$_2$-5 min. This again shows that the double MnO$_2$ layers in the hollow sphere structure leads to a slightly better rate capability.

4. Conclusions

A facile soft templating strategy has been developed for synthesizing hollow spheres of nanocarbon, where a well established hollow structure is achieved for carbon spheres by hydrothermal treatment of α-CD in the presence of F127 as the soft template. This new strategy makes use of the vesicle structures formed by block copolymer PEO−PPO−PEO, with α-CD being threaded on to PEO chains. The resultant hollow spheres of nanocarbon are decorated by PEO chains and other hydrophilic functional groups on the surface, such as carboxyl and hydroxyl groups. As a result, upon pyrolysis at 500 °C in Ar, an all-carbon hollow spherical structure is developed with micro- and meso-pores present in the carbon wall. The hollow spheres of nanocarbon, which exhibit a specific surface area of 379 m^2 g^{-1}, are demonstrated to be an excellent substrate for growth of MnO$_2$ nanocrystallite on their surface by the redox reaction between carbon and MnO$_4^-$. The porous structure of carbon wall allows MnO$_4^-$ ions to diffuse though, which offers the opportunity for developing a double layer hybrid structure consisting of nanocarbon and MnO$_2$. The electrochemical performances of the hollow spheres of nanocarbon−MnO$_2$ hybrid in supercapacitor are evaluated. By comparison, the double layer structure of nanocrystalline MnO$_2$ assembled on both the external and internal surfaces of hollow carbon spheres (HCSA/MnO$_2$-16 h) shows a better performance than that of the supercapacitor working electrode made of hollow carbon with MnO$_2$ deposited on the external surface.

Acknowledgment

Appendix A. Supplementary data

Supplementary data related to this article can be found at http://dx.doi.org/10.1016/j.jpowsour.2013.05.034.

References

[1] G. Wang, L. Zhang, J. Zhang, Chem. Soc. Rev. 41 (2012) 797–828.
[2] J.R. Miller, P. Simon, Science 321 (2008) 651–652.
[3] P. Simon, Y. Gogotsi, Nat. Mater. 7 (2008) 845–854.
[4] B.E. Conway, J. Electrochem. Soc. 138 (1991) 1539–1548.
[5] X. Lang, A. Hirata, T. Fujita, M. Chen, Nat. Nanotechnol. 6 (2011) 232–236.
[6] C.N. Chervin, J.W. Long, N.L. Brandell, J.M. Wallace, N.W. Kucko, D.R. Rolishon, J. Power Sources 207 (2012) 191–198.
[7] R. Saliger, U. Fischer, C. Herta, J. Fricke, J. Non-Cryst. Solids 225 (1998) 81–85.
[8] D.R. Rolison, J.W. Long, J.C. Lytle, A.E. Fischer, C.P. Rhodes, T.M. McEvoy, M.E. Bourg, A.M. Lubers, Chem. Soc. Rev. 38 (2009) 226–252.
[9] X. Zeng, D. Wu, R. Fu, H. Lai, Mater. Chem. Phys. 112 (2008) 1074–1077.
[10] G. Li, Z. Feng, Y. Ou, D. Wu, R. Fu, Y. Tong, Langmuir 26 (2010) 2209–2213.
[11] W. Zhang, J. Chen, Pure Appl. Chem. 81 (2009) 2317–2325.
[12] A.L.M. Reddy, M.M. Shaijumon, S.R. Gowda, P.M. Ajayan, J. Phys. Chem. 114 (2010) 658–663.
[13] Y. Zhu, S. Murali, M.D. Stoller, K.J. Ganesh, W. Cai, P.J. Ferreira, A. Pirkle, R.M. Wallace, K.A. Cychosz, M. Thommes, D. Su, E.A. Stach, R.S. Ruoff, Science 332 (2011) 1537–1652.
[14] L. Zhang, X.S. Zhao, Chem. Soc. Rev. 38 (2009) 2520–2531.
[15] R.W. Pekala, J. Mater. Sci. 24 (1989) 3221–3227.
[16] R.W. Pekala, J.C. Farmer, C.T. Alviso, T.D. Tran, S.T. Mayer, J.M. Miller, B. Dunn, J. Non-Cryst. Solids 225 (1998) 74–80.
[17] R.W. Pekala, R.W. Hopper, J. Mater. Sci. 22 (1987) 1840–1844.
[18] J.C. Lytle, J.M. Wallace, M.B. Sassin, A.J. Barrow, J.W. Long, J.L. Dysart, C.H. Renninger, M.P. Saunders, N.L. Brandell, D.R. Rolison, Energy Environ. Sci. 4 (2011) 1913–1925.
[19] W.S. Baker, J.W. Long, R.M. Stroud, D.R. Rolison, J. Non-Cryst. Solids 350 (2004) 80–87.
[20] A.E. Fischer, M.P. Saunders, J.C. Lytle, D.R. Rolison, J.W. Long, ECS Trans. 6 (2008) 159–164.
[21] J.W. Long, D.R. Rolison, Acc. Chem. Res. 40 (2007) 854–862.
[22] A.-H. Lu, T. Sun, W.-C. Li, Q. Sun, F. Han, D.-H. Liu, Y. Guo, Angew. Chem. Int. Ed. 50 (2011) 11765–11768.
[23] C. Liang, Z. Li, S. Dai, Angew. Chem. Int. Ed. 47 (2008) 3696–3717.
[24] M. Zheng, Y. Liu, S. Zhao, W. He, Y. Xiao, D. Yuan, Inorg. Chem. 49 (2010) 8674–8683.
[25] J.B. Joo, P. Kim, W. Kim, J. Kim, N.D. Kim, J. Yi, Curr. Appl. Phys. 8 (2008) 814–817.
[26] S. Yang, X. Feng, L. Zhi, Q. Cao, J. Maier, K. Müllen, Adv. Mater. 22 (2010) 838–842.
[27] X.C. Chen, K. Kierzek, Z.W. Jiang, H.M. Chen, T. Tang, M. Wojtoniszak, R.J. Kalenczuk, P.K. Chu, E. Borowiak-Palen, J. Phys. Chem. C 115 (2011) 17717–17724.
[28] S.B. Yoon, K. Sohn, J.Y. Kim, C.H. Shin, J.S. Yu, T. Hyeon, Adv. Mater. 14 (2002) 19–21.
[29] B. You, J. Yang, Y. Sun, Q. Su, Chem. Commun. 47 (2011) 12364–12366.
[30] F. Wang, L. Pang, Y. Jiang, B. Chen, D. Lin, N. Lun, H. Zhu, R. Liu, X. Meng, Y. Wang, Y. Bai, L. Yin, Mater. Lett. 63 (2009) 2564–2566.
[31] C. Xiao, X. Chu, Y. Yang, X. Li, X. Zhang, J. Chen, Biosens. Bioelectron. 26 (2011) 2934–2939.
[32] C. Almeida, A.J.G. Zarbin, Carbon 44 (2006) 2869–2876.
[33] Y.D. Xia, R. Mokaya, Adv. Mater. 16 (2004) 886–891.
[34] L. Zhi, J.J. Wang, G.L. Cui, M. Kastler, B. Schmaltz, U. Kolb, U. Jonas, K. Mullen, Adv. Mater. 19 (2007) 1849–1853.
[35] J. Lee, S. Yoon, S.M. Oh, C.-H. Shin, T. Hyeon, Adv. Mater. 12 (2000) 359–362.
[36] L. Lai, G. Huang, X. Wang, J. Weng, Carbon 48 (2010) 3145–3156.
[37] C.D. Liang, K.L. Hong, G.A. Guiochon, J.W. Mays, S. Dai, Angew. Chem. Int. Ed. 43 (2004) 5785–5789.
[38] M. Yang, G. Wang, Colloids Surf. A Physicochem. Eng. Aspects 345 (2009) 121–126.
[39] R.J. White, K. Tauer, M. Antonietti, M.M. Titirici, J. Am. Chem. Soc. 132 (2010) 17360–17363.
[40] N. Wu, S. Kuo, M. Lee, J. Power Sources 104 (2002) 62–65.
[41] J.W. Long, M.B. Sassin, A.E. Fishcher, D.R. Rolison, J. Phys. Chem. C 113 (2009) 17595–17598.
[42] Z. Yang, Y. Zhang, J. Kong, S.Y. Wong, X. Li, J. Wang, Chem. Mater. 25 (2013) 704–710.
[43] Z. Yang, X. Li, J. Wang, Carbon 49 (2011) 5207–5212.
[44] Y. Su, H. Liu, J. Wang, J. Chen, Langmuir 18 (2002) 865–871.
[45] P. Ulanski, W. Pawlowska, S. Kadlubowski, A. Henke, R. Gottlieb, K.F. Arndt, L. Bromberg, T.A. Hatton, J.M. Rosiak, Polym. Adv. Technol. 17 (2006) 804–813.
[46] J. Li, X. Li, Z. Zhou, X. Ni, K.W. Leong, Macromolecules 34 (2001) 7236–7237.
[47] A. Harada, J. Li, M. Kamachi, Macromolecules 26 (1993) 5698–5703.
[48] R.K. Prudhomme, G.W. Wu, D.K. Schneider, Langmuir 12 (1996) 4651–4659.
[49] X.Y. Xiong, K.C. Tam, L.H. Gan, Macromolecules 36 (2003) 9979–9985.
[50] S.W. Lee, J. Kim, S. Chen, P.T. Hammond, Y. Shao-Horn, ACS Nano 4 (2010) 3889–3896.
[51] Z.-S. Wu, W. Ren, D.-W. Wang, F. Li, B. Liu, H.-M. Cheng, ACS Nano 4 (2010) 5835–5842.
[52] S. Devaraj, N. Munichandraiah, J. Phys. Chem. C 112 (2008) 4406–4417.
[53] Z. Lei, J. Zhang, X.S. Zhao, J. Mater. Chem. 22 (2012) 153–160.
[54] L. Mao, K. Zhang, H.S.O. Chan, J. Wu, J. Mater. Chem. 22 (2012) 1845–1851.
[55] S. Ching, D.J. Petrovay, M.L. Jorgensen, S.L. Suib, Inorg. Chem. 36 (1997) 883–890.
[56] J. Wang, Y. Yang, Z. Huang, F. Kang, J. Power Sources 204 (2012) 236–243.
[57] W. Wei, X. Cui, W. Chen, D.G. Lvey, Chem. Soc. Rev. 40 (2011) 1697–1721.
[58] Q. Li, J.M. Anderson, Y.Q. Chen, L. Zhai, Electrochim. Acta 59 (2012) 548–557.
[59] G.H. Yu, L.B. Hu, M. Vosgueritchian, H.L. Wang, X. Xie, J.R. McDonough, X. Cui, Y. Cui, Z.N. Bao, Nano Lett. 11 (2011) 2905–2911.